Cryogenics 91 (2018) 103–111

Contents lists available at ScienceDirect

Cryogenics

journal homepage: www.elsevier.com/locate/cryogenics

Determining solid-fluid interface temperature distribution during phase change of cryogenic propellants using transient thermal modeling

K. Bellur[a], E.F. Médici[a], J.C. Hermanson[b], C.K. Choi[a], J.S. Allen[a,*]

[a] Michigan Technological University, 1400 Townsend Drive, Houghton, MI, USA
[b] University of Washington, Seattle, WA, USA

ARTICLE INFO

Keywords:
Cryostat
Transient thermal model
Contact resistance
Wall temperature distribution
Contact line evaporation

ABSTRACT

Control of boil-off of cryogenic propellants is a continuing technical challenge for long duration space missions. Predicting phase change rates of cryogenic liquids requires an accurate estimation of solid-fluid interface temperature distributions in regions where a contact line or a thin liquid film exists. This paper described a methodology to predict inner wall temperature gradients with and without evaporation using discrete temperature measurements on the outer wall of a container. Phase change experiments with liquid hydrogen and methane in cylindrical test cells of various materials and sizes were conducted at the Neutron Imaging Facility at the National Institute of Standards and Technology. Two types of tests were conducted. The first type of testing involved thermal cycling of an evacuated cell (dry) and the second involved controlled phase change with cryogenic liquids (wet). During both types of tests, temperatures were measured using Si-diode sensors mounted on the exterior surface of the test cells. Heat is transferred to the test cell by conduction through a helium exchange gas and through the cryostat sample holder. Thermal conduction through the sample holder is shown to be the dominant mode with the rate of heat transfer limited by six independent contact resistances. An iterative methodology is employed to determine contact resistances between the various components of the cryostat stick insert, test cell and lid using the dry test data. After the contact resistances are established, inner wall temperature distributions during wet tests are calculated.

1. Introduction

One of the limiting factors in long duration space missions is the ability to maintain propellant storage depots. Computational Fluid Dynamics (CFD) along with a lumped parameter treatment of the vapor has been used to study pressurization in cryogen tanks and these have shown that a thin (≈1 mm) liquid layer separating the vapor phase from the wall is obtained [1–4]. Propellants exist as liquid-vapor mixtures that constantly undergo phase change. Liquid-vapor phase change is a complex, multi-scale problem and kinetic theory has provided the framework for modeling evaporation/condensation for over a century. Classical kinetic theory is a statistical description of the behavior of gases based on velocities of the constituent molecules. Although kinetic models have shown to be very effective in capturing phase change, the use of the models is still limited due to the fact that kinetic theory only describes the maximum phase change flux possible for a given thermodynamic situation [5]. In reality, the phase change flux may be lower than the maximum value depending on the molecular species under consideration [6]. Evaporation and condensation coefficients were introduced by Knudsen [7] in order to account for the deviation from the maximum phase change rate. Evaporation and condensation coefficients are often set equal to each other and referred to as the accommodation coefficient. CFD modeling of propellant behavior utilizes the accommodation coefficient as an input to capture phase change [1,8,9]. This is particularly challenging due to the lack of available evaporation/condensation coefficients and the inability to sufficiently resolve local thermodynamics at the liquid-vapor interface [10–13]. These coefficients must be determined experimentally [14].

At an evaporating or condensing meniscus, the normal stress in the bulk liquid is primarily influenced by interface curvature. Far from the meniscus, the adsorbed region consists of a nanoscale, non-evaporating layer of liquid molecules where intermolecular forces dominate. Between these two exists a transition film region in which the normal stress is affected by both intermolecular forces and interface curvature. For non-polar/wetting liquids, 60–90% of the evaporation occurs in the thin film region close to the wall [15–21].

Most thin film evaporation models use a constant wall temperature condition in the transition film region [16,18–20,22–27]. However, due

* Corresponding author.
E-mail address: jstallen@mtu.edu (J.S. Allen).

https://doi.org/10.1016/j.cryogenics.2018.02.009
Received 12 July 2017; Received in revised form 26 January 2018; Accepted 27 February 2018
Available online 09 March 2018

to non-uniform evaporation there exists temperature gradients along the wall near the transition region as demonstrated by Stephan and Busse [28]. The non-uniform wall temperature can generate thermocapillary stresses at the interface, which in turn affects the local normal stress in the liquid and subsequently the evaporation rate. In order to accurately capture the thermophysics of evaporation at a contact line, thermal boundary conditions should be representative of local temperature distributions along the solid-liquid interface. Accounting for the non-uniform wall temperature is a key factor to accurately model phase change and ultimately calculate the evaporation and condensation coefficients. Details of calculation of evaporation and condensation coefficients using kinetic theory are described elsewhere [12].

This paper represents one piece of the overall methodology; a thermal model that serves to bridge the macroscale experiment observations with the micro-scale phase change modeling. The goal of this thermal model is (1) determine the rate and mode of heat transfer to the cryogenic liquid in the test cell and (2) translate discrete exterior surface temperature measurements to an interior wall temperature distribution suitable for use in the microscale transport model.

2. Cryogenic phase-change experiments

Cryogenic phase change experiments with hydrogen and methane were conducted, using a 70-mm-cryostat at the Neutron Imaging Facility at the National Institute of Standards and Technology (NIST). The experiments were conducted at absolute pressures between 100 and 210 kPa, corresponding to saturation temperatures between 15 K and 30 K for hydrogen and 100–120 K for methane.

Fig. 1(a) illustrates the components of the cryostat. Test cells are suspended in a sample well, below the cryostat using a 720-mm-long sample holder. The test cell is mounted to the bottom of the sample holder via a flange that includes a gas exchange port to allow hydrogen or methane vapor to be introduced into the test cell. The flange is attached to the test cell using an indium seal and secured in place with six screws. The sample holder is sealed at the top of the cryostat with ports for sensor leads and a cryogen vapor feed line. Radiation baffles on the sample holder minimize heat transfer from the top of the cryostat. The temperature in the sample well is controlled using a combination of an electric heater and liquid helium phase change passing through an expansion valve. Helium boiling occurs continuously and the heater is used to maintain sample well temperatures above the helium boiling point.

The cryostat heater is attached to a copper annulus that is in contact with the bottom radiation baffle. The heat path from the copper block to the test cell is through the bottom radiation baffle, sample holder, and flange. Low pressure helium gas introduced into the sample well provides a parallel conduction path between the heater block and the test cell. The annular contact between the copper heater block and the bottom radiation baffle is approximately 1 mm wide. The lower radiation baffles are spring loaded to allow for the test cell position to be adjusted within the sample well. As a result, the contact resistance between the lower radiation baffle and the copper heater block changes with each test configuration.

Fig. 1(b) illustrates one of the test cells that has a 10-mm-diameter bore. Four Lakeshore silicon diode DT-670 sensors were used to record temperature at various locations. One sensor (s1) was suspended in the helium exchange gas approximately 1 cm from the test cell wall. The remaining three sensors (s2–s4) were mounted on the external surface of the test cell. The sensors were secured to the outside of the test cell using 316 SS wire with spring-wire tensioners. The temperatures sensors were connected to a Lakeshore 340 temperature controller. The lower flange mount on the sample holder houses a fifth Si-diode temperature sensor (Scientific Instruments SI-410b). The copper heater block contains an NTC RTD X45720 sensor hereby referred to as the 'heater sensor'. The heater and the sample holder sensors were connected to a Lakeshore 331 temperature controller. The heater

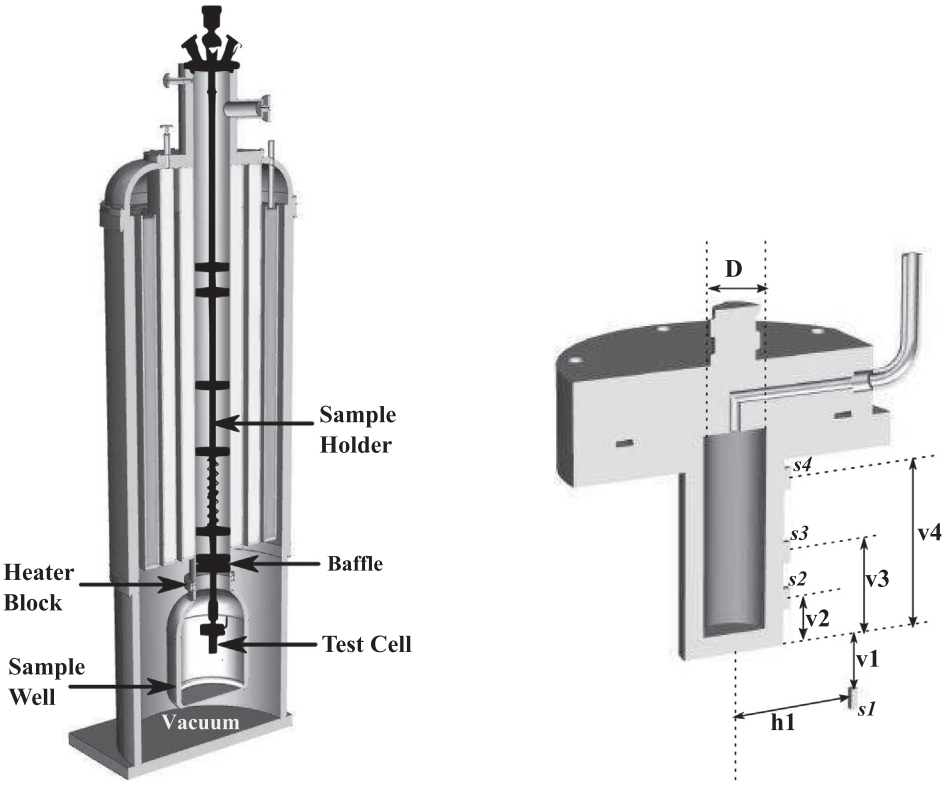

(a) Cryostat configuration (b) 10-mm diameter test cell with sensor location

Fig. 1. Hardware configuration for cryogenic phase change experiments. (a) Cryostat with test cell suspended in sample well. (b) Illustration of the 10-mm diameter test cell. s1, s2, s3, and s4 are the temperature sensors. The location of each (v1, v2, v3, v4) are relative to the bottom exterior surface of the test cell.

Table 1
Test cells used in the hydrogen and methane experiments and the sensor locations as indicated in Fig. 1. All dimensions are in mm.

Experiment	Material	D	h1	v1	v2	v3	v4
Hydrogen	SS 316L	10	20	10	5	12	21
	Al 6061	30	n/a	n/a	7	16	25
	Al 6061	10	20	10	7	14	25
Methane	Al 6061	10	20	10	7	14	25

temperature was set and maintained using an auto-tuned PID control system built into the Lakeshore 331. Gas manifold pressure was logged using a Mensor DPG 15000. The reader is directed to the authors' previous publications for additional details on the experimental setup and cryostat operation [12,29].

Two experimental campaigns are included in this discussion; tests with hydrogen and with methane. Three different test configurations were used in the hydrogen campaign (Table 1). The 10 mm Al 6061 cell was reused in the methane campaign. Sensor locations on the test cells, listed in Table 1, were measured after assembly. Two types of tests were conducted with each test cell. The first was thermal cycling of an evacuated cell referred to as "dry" tests. The second was controlled phase change with cryogenic liquid referred to as "wet" tests.

Dry tests were conducted with a hard vacuum inside the test cell. The cryostat heater was thermally cycled though a range of temperatures and the corresponding temperatures on the test cell, sample holder, heater, and helium gas in the sample well were recorded. Prior to each dry test, the test cell assembly was maintained in thermal equilibrium. Once a steady state temperature was attained, data logging was initiated and the temperature set point on the heater was increased. Temperatures from the four Lakeshore sensors, the sample holder sensor, the heater temperature and the heater power were logged at 1 Hz. After the test cell assembly reached the new equilibrium state, the heater set point was lowered.

The results from thermal cycling of evacuated cells tested in both the hydrogen and methane experiments are shown in Fig. 2. Sensor s1 for the 30 mm Al cell setup was damaged during the assembly, hence helium temperature data is unavailable for this set of experiments. Dry test experiments in the methane campaign were carried about at temperatures between 90 K and 110 K (saturation temperature of methane corresponding to 100–210 kPa). At these temperatures, the thermal transients are longer than those observed in the 20–30 K range during the hydrogen campaign. This delayed response is due to increased resistances to the heat conduction path between the baffle and the test cell as well as significant changes in material properties with temperature.

The source of hydrogen for the wet tests was 99.9995% pure, water vapor < 5 ppm, N2 < 2 ppm, O2 < 1 ppm, all others undetectable. The methane purity was 99.97%. Vapor was introduced through the feed line in the test cell at a preset pressure controlled by the gas manifold outside the imaging facility. The vapor was condensed inside the test cell by lowering the cryostat temperature below the saturation temperature corresponding to the manifold pressure. After the condensation experiments were complete, the cryostat temperature was increased above the saturation temperature to induce evaporation. During the methane campaign, it was observed that the time to a steady state thermal response upon unit change in temperature was at least 2 orders of magnitude greater than that seen during the hydrogen campaign. The higher temperatures for methane phase change, construction of the cryostat and corresponding changes in material properties result in wait times of several hours while access to the neutron beam was limited to a few days. Hence, in the interest of time, once a steady

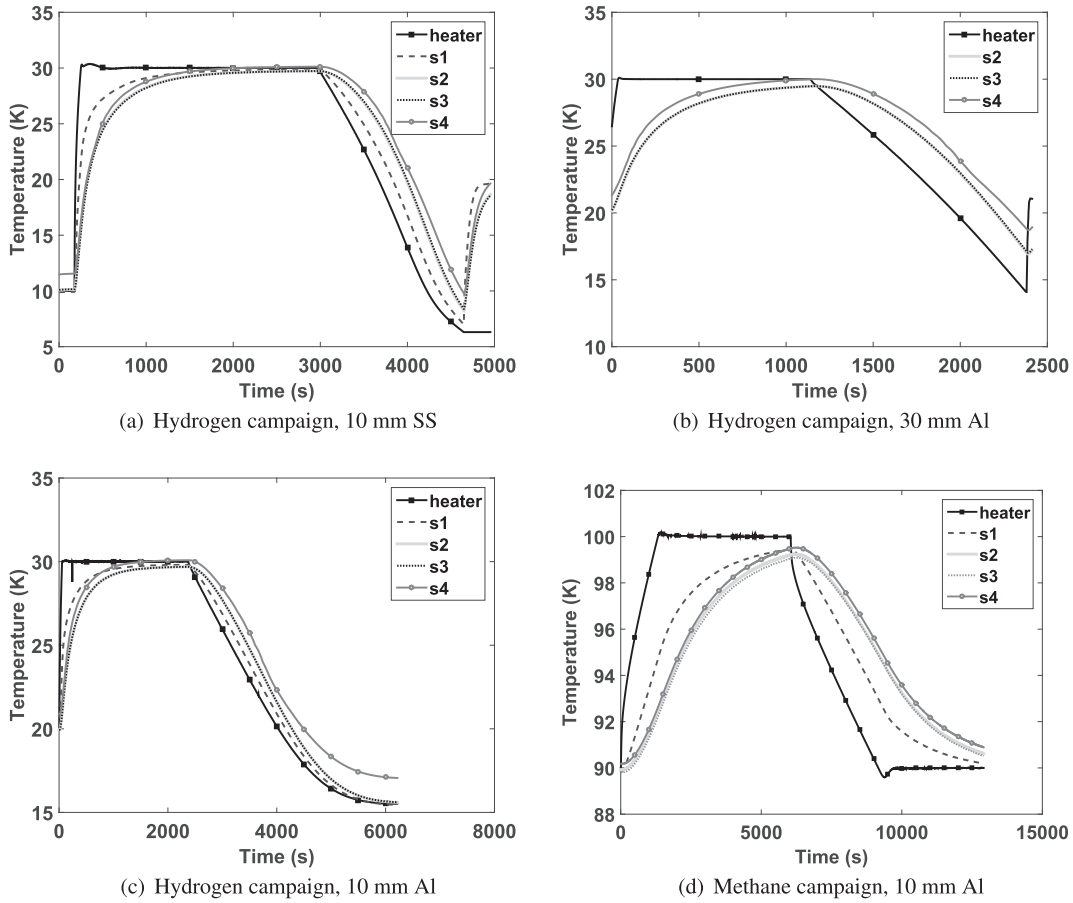

(a) Hydrogen campaign, 10 mm SS
(b) Hydrogen campaign, 30 mm Al
(c) Hydrogen campaign, 10 mm Al
(d) Methane campaign, 10 mm Al

Fig. 2. Temperatures during thermal cycling of "dry" cell tests. "Heater" refers to the temperature sensor located in the cryostat heater block.

temperature was attained, it was held constant and the manifold pressure was changed instead to induce condensation and evaporation.

3. Transient thermal modeling of cryostat

The objective of the ANSYS/Fluent thermal model is to extract the inner wall temperature distribution from the experimentally measured discrete outer wall temperatures. An axisymmetric model was built using the ANSYS design modeler™. The computational domain encompassed the sample holder from the bottom radiation baffle to the test cell, the cryostat heater, the sample well and the helium exchange gas. Fig. 4 is the axisymmetric computational domain with the symmetry axis in the *x*-direction. The components are individually modeled as separate entities so each component could be assigned independent thermal properties and boundary conditions. Shadow walls are used at all component interfaces to transfer heat and model thermal contact.

Data from the evacuated (dry) thermal cycling tests are used to tune the contact resistances in the transient thermal model. Though the temperature change during thermal cycling is modest at 10–20 K, values thermal conductivity and specific heat for materials used in the experiments change by an order of magnitude. Temperature dependent conductivity and specific heat for aluminum 6061 [30,31], copper [30,32], stainless steel 316 [31,33] are used in the thermal model. The change in density of solids due to thermal contraction from 300 K was accounted for using data provided by [34]. For the helium exchange gas in the sample well, temperature dependent data for viscosity, specific heat and thermal conductivity is used [35–37]. Correlations between thermal conductivity, specific heat and temperature for these materials are shown in Fig. 3. These material properties are tabulated in a lookup table that is read by the ANSYS/Fluent model.

A quad dominant mesh is generated for the domain with size refinement at all contact interfaces. A coarse mesh was initially built and the mesh size in the all the zones was monotonically reduced. The minimum spatial resolution in the test cell outer wall was set to be 50 μm. Increasing the number of elements beyond 19,000 resulted in the relative mean square error of the transient temperature profile $<10^{-10}$ in the s1 and s2 locations and a maximum relative change less than 100 μK. The optimal trade-off between accuracy and computational overhead was found with using 19,566 elements. The average computational time for a typical dry test is about 8 h when run in parallel on 16 cores.

The heater temperature logged during the experiments is used as a boundary condition with all outer walls of the domain insulated. For the dry tests, the interior of the test cell is evacuated. Radiation from the sample well to the test cell is less than 5% of the conductive heat transfer with a perfect vacuum in the sample well. The presence of helium gas would only reduce the amount of heat transfer due to radiation. Therefore, radiation has been neglected in the thermal model. The pressure of the helium exchange gas was approximately 400 Pa. This varied from test-to-test, but not enough to significantly alter the thermal properties of helium in the sample well.

4. Contact resistances

Initial simulations with perfect thermal contact at all the solid-solid interfaces resulted in steady-state predictions approximately four times faster than the experimental values. Six locations were identified as having a significant contact resistance. Five of these resistances are in the conduction path from the heater to the sample holder (stick) and test cell. The sixth resistance is in the conduction path through the helium exchange gas.

Wall-to-Baffle: The bottom radiation baffle of the sample holder is in contact with the heater on a 1 mm wide annulus with an inside diameter of 68 mm. The baffle is spring loaded to ensure good contact and a direct heat conduction path. A second heat conduction path exists between the baffle and the cryostat wall. The outer circumference of the baffle is 69 mm and the cryostat has a 70 mm bore. The gap between the baffle and cryostat wall is filled with helium that is in communication with the sample well. The helium thermal conductivity is 0.01–0.03 W/m K in the temperature range of 5–20 K [35]. The parallel heat path from the heater-to-baffle and cryostat-to-baffle is modeled as a single contact resistance.

Baffle-to-Sample Holder: The radiation baffle is attached to a spring-loaded sleeve that allows for adjusting the vertical location of the test cell within the sample well. The baffle is attached to the sleeve using a cryogenic epoxy (Stycast 2580FT) with a thermal conductivity of 1.3 W/m K at room temperature and 0.064 W/m K at 4.2 K. Helium, in communication with the sample well, resides in the gap between the baffle sleeve and sample holder. The combined serial resistances of the baffle to epoxy to sleeve to helium to sample holder is modeled as a single contact resistance.

Sample Holder-to-Sensor: The sample holder includes a threaded element that houses a si-diode temperature sensor (Scientific Instruments SI-410b). Data from the sample holder temperature sensor is not used in this analysis because of the large uncertainty with this particular sensor. Helium that is in communication with the sample well resides within the sensor cavity so that there is a parallel heat path along the axis of the sample holder. Heat is conducted through the solid–solid contact and through the solid-helium-solid contact. This is modeled as a single contact resistance.

Sensor-to-Spacer: During the methane campaign, threaded aluminum 6061 spacers were added between the sample holder and test cell flange in order to increase the contact pressure between the heater block and baffle and to provide additional extension of the test cell within the

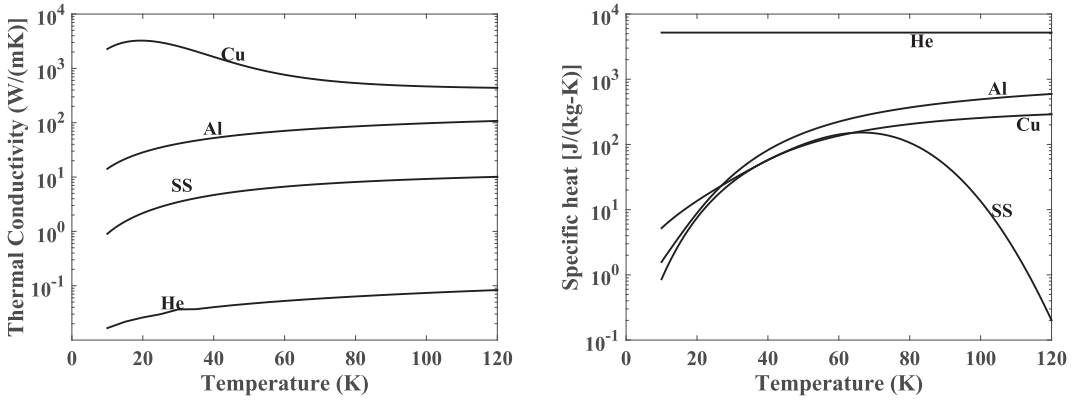

(a) Conductivity (b) Specific heat

Fig. 3. Temperature dependent thermal properties.

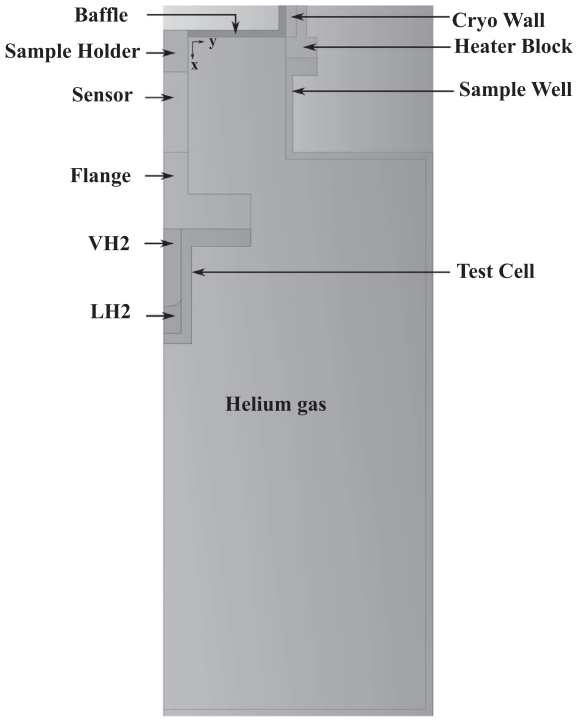

Fig. 4. Computational domain of the thermal model.

sample well. The conduction path from the sensor housing to spacers (if present) is modeled as a single contact resistance.

Spacer-to-Flange: The flange sealing the top of the test cell and containing the gas passage is attached to either a spacer or the sensor housing via a threaded connection. The diameter of the threaded contact is 15 mm. The sensor housing and spacers are aluminum 6061. The test cell flange (lid) is 316L stainless steel.

Flange-to-Test Cell: The test cell is bolted to the flange using six 4–40 aluminum bolts and sealed against leakage using an indium seal. Fig. 1(b) illustrates the test cell to flange geometry for the 10-mm-diameter test cells. The contact area between the test cell and flange varied with each test cell.

Heater-to-Sample Well: The sample well is bolted to the copper heater block and provides a secondary heat conduction path from the sample well wall through the helium exchange gas to the test cell. The contact between the heater block and the sample well is modeled as a contact resistance.

Thermal contact resistances are modeled using the thin wall conduction model in FLUENT, which solves a 1D conduction equation between the two shadow walls that define the interface. The thin wall conduction model requires specification of a conductivity for an imaginary material of interface and a wall thickness. Initially all contact interfaces are set to a thickness of 1 mm and a conductivity of 0.1 W/m K. An iterative methodology is used to adjust the shadow wall thickness and thermal conductivity for the six contact resistances.

5. Determining contact resistances from dry cell thermal cycling

The transient axisymmetric model is evaluated using ANSYS FLUENT to solve the equations of continuity, momentum and energy. A pressure based approach is employed and the pressure velocity coupling is achieved using the Corrected Semi Implicit Pressure Linked Equation with a zero skewness factor. The pressure, density, momentum and energy is evaluated using the body force weighted method, second order upwind, second order upwind and third order MUSCL methods respectively. A first order implicit time stepping method was used for temporal resolution. A time step of 1 s was deemed to suffice since the time to steady state is on the order of 1000 s. The default under relaxation parameters were used in the simulation and the residuals were set to 10^{-2} for continuity, 10^{-6} for x and y velocity components and 10^{-16} for the energy equation. Approximately 50 iterations are necessary for convergence at each time step. The convergence criteria was set at a minimum of 3 order reduction in the residuals of continuity, velocities and energy.

A manual optimization method is used to determine a set of resistances that accurately captured the transient temperatures in both the helium gas (s1) the exterior test cell surface (s2–s4). The *Wall-to-Baffle* resistance was set to that of a 1 mm wide annulus filled with helium gas at the heater temperature. The conjugate heat transfer encountered here allows for the heat to propagate through a parallel path (helium gas) if the resistance in the primary path (conduction through the baffle-sample holder) is high. The highest resistance is at the baffle-sample holder interface due to the sleeve and the cryogenic epoxy. Hence, the *Baffle-to-Sample Holder* resistance was first increased to minimize the difference in time constants between the simulation and experiments. The time constants could be matched to within 30%, but further increase in resistance beyond a certain value had no effect on the time constant. The *Wall-to-Baffle* resistance was fixed at the value that resulted in less than 1% relative change of the time constant. Then, the *Sample Holder-to-Sensor* and the *Sensor-to-Flange* resistances were increased equally until the relative time constant change was less than 1%. At this stage, the time constants could be matched to within 10%. The remaining two resistances: *Flange-to-Test Cell* and *Heater-to-Sample Well* are determined through a parametric least squares routine by comparing the simulation results to the experimental helium gas temperature (s1) and the outer wall temperature (s2). The process is terminated when the simulated time constant is within 1% of the experimental data and the simulation temperatures are within the sensor uncertainty (±0.25 K). The error in the heater temperature was ±0.1 K. As a result, the relative uncertainty in the reported resistance parameters are <1.3%. The contact resistances for the hydrogen and methane campaigns are listed in Tables 2 and 3, respectively.

In the methane simulations, the *Sensor-to-Spacer* and *Spacer-to-Flange* resistances are changed in lieu of the *Sensor-to-Flange* resistance.

Table 2
Contact resistances determined from the hydrogen experiments. Units for contact area are mm^2, conductivities are W/m K, and resistances are K/W.

	Contact interface:	Wall - baffle	Baffle - sample holder	Sample holder – sensor	Sensor – flange	Flange – testcell	Heater – sample well
	Contact area	4398.230	87.965	153.938	153.938	1178.097	2233.672
10 mm SS (20–30 K)	Conductivity	0.020	0.020	0.100	0.100	0.300	0.300
	Resistance	11.3	852	65	65	2.83	1.49
30 mm Al (20–30 K)	Conductivity	0.025	0.025	0.100	0.100	0.350	0.300
	Resistance	10.0	728	65	65	2.43	1.49
10 mm Al (15–30 K)	Conductivity	0.025	0.025	0.100	0.100	0.250	0.250
	Resistance	9.1	682	65	65	3.34	1.79

Table 3
Contact resistances determined from the methane experiments with the 10 mm Al cell. Units for contact area are mm^2, conductivities are W/m K, and resistances are K/W.

Contact interface:	Wall – baffle	Baffle – sample holder	Sample holder – sensor	Sensor – spacer	Spacer – flange	Flange – testcell	Heater – sample well
Contact area (mm^2)	4398.23	87.96	153.94	153.94	153.94	1178.10	2233.67
Conductivity (W/m K)	0.07	0.07	0.10	0.10	0.10	0.40	0.40
Resistance (K/W)	3.25	244	65	65	65	2.12	1.12

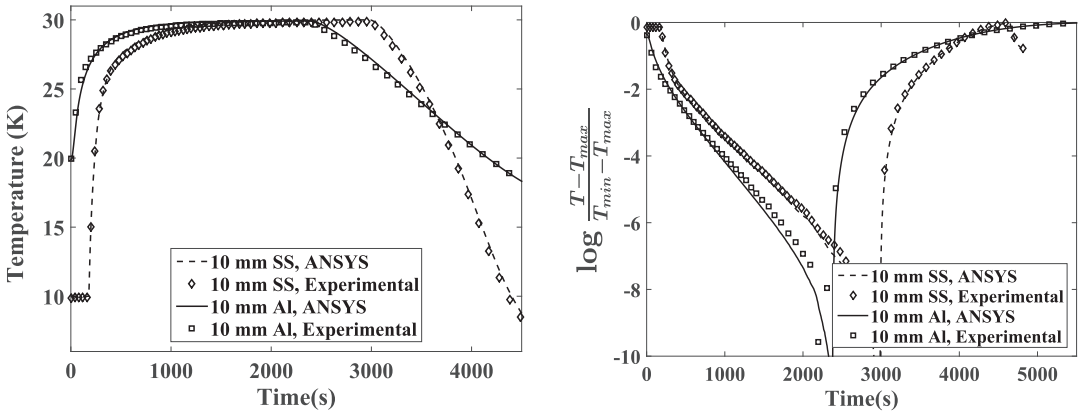

(a) Sensor s1 (b) Sensor s1, log-temperature difference

Fig. 5. Comparison of simulation and hydrogen experiments for sensor s1.

This procedure provides one of several possible sets of solutions that results in accurate tracking of transient temperatures. To obtain a unique solution, experimental temperatures at several points in the conduction path (for example, baffle, flange, sample holder, etc.) are needed.

Figs. 5 and 6 compare the simulation results to the experimentally measured temperatures from the hydrogen dry cell experiments. Fig. 5(a) is of sensor s1 on the 10-mm SS 316 test cell and the 10-mm AL 6061 test cell. Fig. 5(b) is the same comparison shown as a log-temperature difference, in which the accuracy of the model to capture the time response of the cryostat assembly is evident. Fig. 6(a) and (b) are the same comparison for sensor s2 with the addition of the 30-mm AL 6061 test cell. Results for sensor s3 are not shown because these are identical to sensor s2. Fig. 7(a) and (b) compare the simulation results to the experimentally measured temperatures from the methane dry cell experiments. The marker size in Figs. 5–7 is equivalent to the measurement uncertainty at the corresponding temperature.

Variation in the exchange gas pressure had little effect on the transient response. Helium exchange gas pressure was varied in the model from 10 Pa up to 1 kPa and the resulting transient temperatures at the s2 location had a relative mean square error less than 10^{-10} and a maximum relative change less than 100 μK. Maximum helium velocities in the simulations are on the order of 10^{-3} m/s with corresponding Rayleigh number (non-dimensional number that represents the ratio of buoyant forces to viscous forces) less than 100. In order to test the role of convection in the sample well, the helium was modeled as a solid with a constant density and temperature dependent properties of helium gas. These simulations yielded similar results as the convective cases. Variation in temperatures between fluid and solid simulations are less than 100 μK. Modeling the helium exchange gas as a solid decreases the computational time of the simulations by 15%.

6. Thermal modeling for phase change experiments

Once the dry cell thermal cycling tests were completed, hydrogen or methane was condensed in the test cell to begin the phase change (wet) tests. The hardware configuration remained the same. As such, the contact resistances determined from the dry cell thermal cycling data remain valid for the wet tests. Fig. 8 illustrates the boundary conditions for the computational domain inside the test cell. On the vapor side of

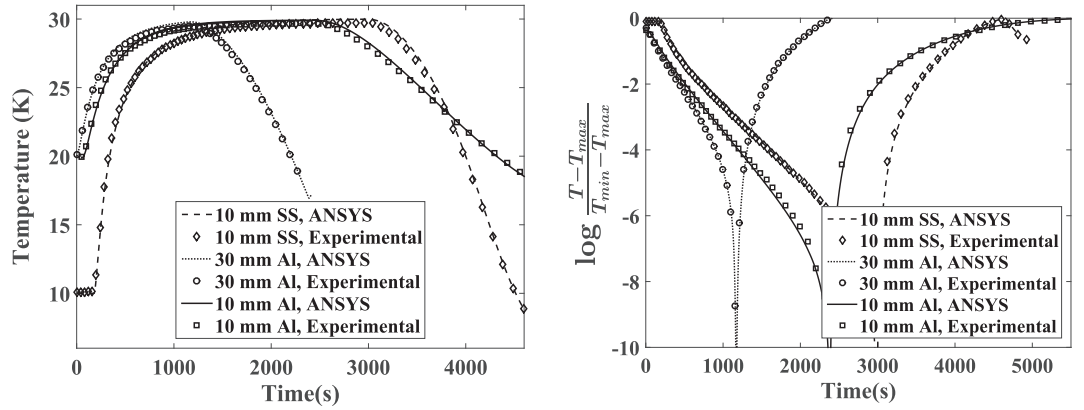

(a) Sensor s2 (b) Sensor s2, log-temperature difference

Fig. 6. Comparison of simulation and hydrogen experiments for sensor s2.

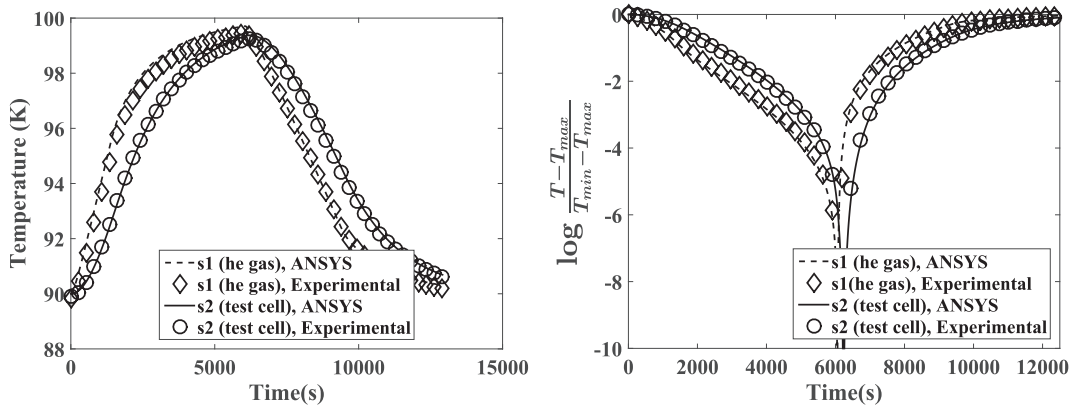

(a) Sensors s1 and s2 (b) Sensors s1 and s2, log-temperature difference

Fig. 7. Comparison of simulation and methane experiments for sensors s1 and s2.

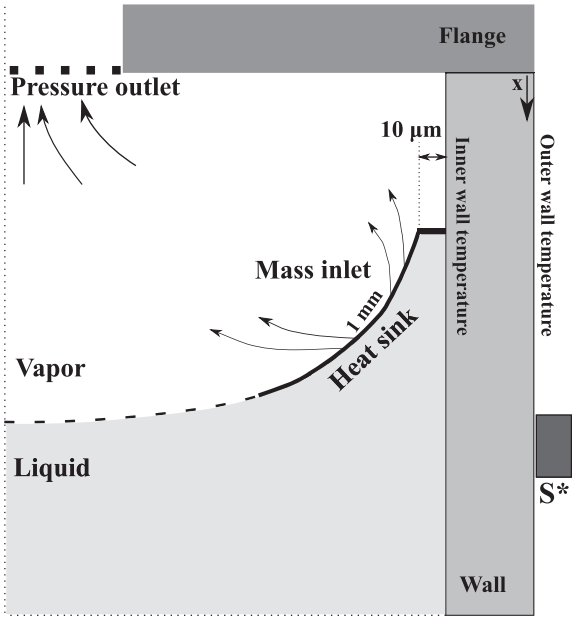

Fig. 8. Boundary conditions for vapor domain and liquid-vapor interface.

the test cell domain, a uniform mass flux boundary condition and a constant pressure condition corresponding to saturation at the test cell exit are imposed. Contact resistances determined from the dry cell thermal cycling data are used and the heater temperature serves as a thermal boundary condition for heat flux to the test cell.

For all hydrogen tests, the measured evaporation rates for each run were between 0.4 and 0.6 mg/s, corresponding to a bulk meniscus velocity of 14–25 μm/s, which remained constant throughout the evaporation test. The evaporation rate is slow with a Peclet number less than 10^{-2}, indicating that the dominant mode of heat transfer to the test cell during phase change is conduction. Because the liquid-vapor in the test cell is near thermal equilibrium, the liquid domain is treated as a solid with temperature dependent properties corresponding to liquid hydrogen [38,39]. Thermodynamic properties of both liquid and vapor are determined using the fundamental equation of state described by [40].

Simulation of liquid hydrogen evaporation presented here correspond to the 10 mm Al test cell. During evaporation testing the manifold pressure corresponds to a saturation temperature of 21 K while the heater was set to 23 K. The liquid-vapor interface profile and location is then imported into ANSYS design modeler™and a cubic spline fit is performed. Meshing the interface as extracted from the images proved to be a challenge especially when the film thickness becomes less than 1 μm. In order to avoid a highly skewed mesh at the three phase contact point, the liquid film was terminated at 10 μm as shown in Fig. 8. Computational expense increased by two orders of magnitude for each order of magnitude reduction in film thickness less than 10 μm. The mesh for all regions outside the test cell was the same as in the dry model. Liquid and vapor regions inside the cell have a quad-dominant mesh with nominal element size of 100 μm in the bulk region gradually reducing to 10 μm near all interfaces (solid-liquid, liquid-gas and gas-solid). Further reduction in the mesh size results an relative mean square error $<10^{-10}$ in the inner wall temperature and a maximum relative change <100 μK.

Experimentally measured meniscus profiles did not exhibit any hysteresis during recession and the meniscus shape remained the same during evaporation and condensation tests [12,29,41]. Therefore, phase change is modeled as quasi-steady with a fixed interface location. Heat loss at the wall due to evaporation was modeled using a uniform heat-sink on the liquid side of the liquid-vapor interface. The rate of energy and mass exchange during evaporation is determined from the experimentally measured rate of meniscus recession within the test cell. Although the magnitude of the total heat loss is known from macroscale observations, the appropriate location of the heat sink in the thermal model is not. Thin film evaporation modeling suggests that a majority of the evaporative flux occurs in the contact line region [15–21]. For these simulations the evaporative flux is uniformly distributed along a 0.95 mm section of the contact line region beginning at the 10 μm termination point. For a length over which the evaporative flux is distributed between 0.90 and 1.2 mm, the thermal model results do not change. If the length is increased beyond 1.2 mm the prediction of the temperature at sensor s1, located in the helium space, begins to deviate from experimental values.

The experimental inputs to the model are the temperature of the heater during evaporation, manifold pressure, and rate of evaporation. The heater temperature is held constant at 23 K. The manifold pressure is held constant at 121.5 kPa (abs), which corresponds to a saturation temperature of 21 K. And the evaporative mass rate is 0.556 mg/s. The steady-state temperature contours for the entire computational domain and velocity streamlines in the vapor domain are shown in Fig. 9. Within the test cell, liquid, vapor and solid temperatures are within 0.1 K of saturation. Temperature variations between the liquid, vapor and/or test cell wall is lower than resolution of the Si diode temperature sensors used but within the resolution of the thermal model. The maximum velocity in the hydrogen vapor is less than 0.02 m/s corresponding to a Reynolds number below 300.

The inner and outer wall temperature distributions are shown in Fig. 10. The distance is relative to the bottom of the test cell as shown in Fig. 1(b). The 10 μm thin film termination is located at 10 mm. Outer

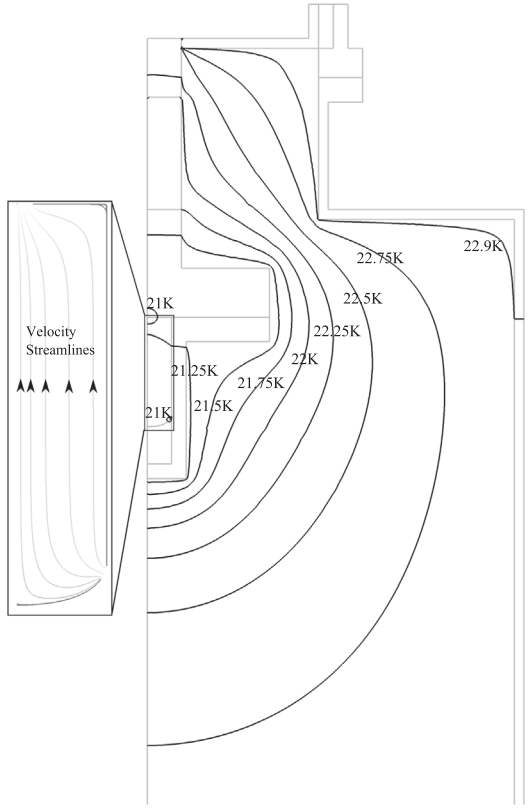

Fig. 9. Temperature contour in the sample well and velocity streamlines in the vapor space of the test cell during steady state phase change of liquid hydrogen saturated at 21 K. The heater was set at 23 K. Streamlines emanate from the contact region and terminate at the exit of the test cell. Vapor velocities are less than 2 cm/s.

wall temperatures are within the measured temperature uncertainty for sensors s1-s3 as shown in Fig. 10(a), where s1 is located in the helium exchange gas. Experimental readings from sensor s4 are approximately 0.5;K above that predicted by the thermal model. This difference is due to a temperature dependent thermal offset in the calibration of sensor s4, which can also be observed in the dry cell thermal cycling data in Fig. 2. Sensor s4 consistently indicates a 0.5 K higher temperature as compared to the other 3 sensors even under equilibrium conditions. When corrected for this bias, the predicted temperature at the s4 location also lies within the sensor uncertainty. The variation in the inner wall temperatures due to the uncertainty in resistance values are $<10^{-3}$ K.

The inner wall distribution, shown in Fig. 10(b), exhibits a minimum temperature in the contact line region. From the contact line region towards the heater, the temperature increases linearly as expected,indicating steady conduction. From the contact line region towards the bottom of the test cell, the temperature also increases, though not strictly linearly. The temperature variation in the contact line region is small in magnitude, approximately 10^{-2} K, but the distance over which this variation occurs is also small, approximately 50 μm. As a result, the temperature gradient in the contact line region is on the order of 10^3 K/m, which is significant considering the liquid film thickness at this location is on the order of 0.1–1 μm.

At these thicknesses the temperature gradient along the liquid-vapor interface will mirror that along the solid-liquid interface (wall) because of the short heat conduction path. Significant thermocapillary stresses will occur even in a pure liquid-vapor system due to the localization of evaporative flux. While soluto-capillary interface stresses have been predicted for evaporation of binary mixtures [18], thermocapillary interface stresses are not thought to occur in single-component liquid-vapor phase change because localized evaporation and condensation should equilibrate any local temperature variation on the interface. Modeling results of thin liquid films tend to validate or presume this assumption, but these same models impose a constant wall temperature condition [15–18,20]. The sustained non-uniformity of the wall temperature distribution as shown in this thermal model has the potential to maintain thermocapillary stresses on the liquid-vapor interface even in pure liquid-vapor systems in the contact line region. For this temperature gradient, thermocapillary stresses will tend to suppress capillary flow into the contact line region; thereby decreasing the overall evaporation rate.

7. Summary and conclusion

In summary, a thermal model of heat transfer of a cryostat environment has been developed that accurately captures steady state and transient temperatures. Accurate modeling is complicated by the number of contact resistances that can change between tests and the temperature dependency of material properties. The contact resistances were determined through an iterative method comparing predicted temperatures with measured temperatures on the exterior of an evacuated test cell undergoing thermal cycling. The purpose of the thermal model is to twofold. Firstly, it is to determine the temperature distribution on the interior of the test cell. Secondly, it is to establish an accurate prediction of the rate of conduction heat transfer along the sample holder and through the helium exchange gas during condensation/evaporation of liquid hydrogen or liquid methane.

The thermal model was first used to determine the effective contact resistances for each test configuration, which covered two temperature ranges (hydrogen and methane) and four test cell configurations. Then the thermal model was applied to hydrogen evaporation at 21 K in the 10-mm diameter Al test cell to predict inner and outer wall temperature

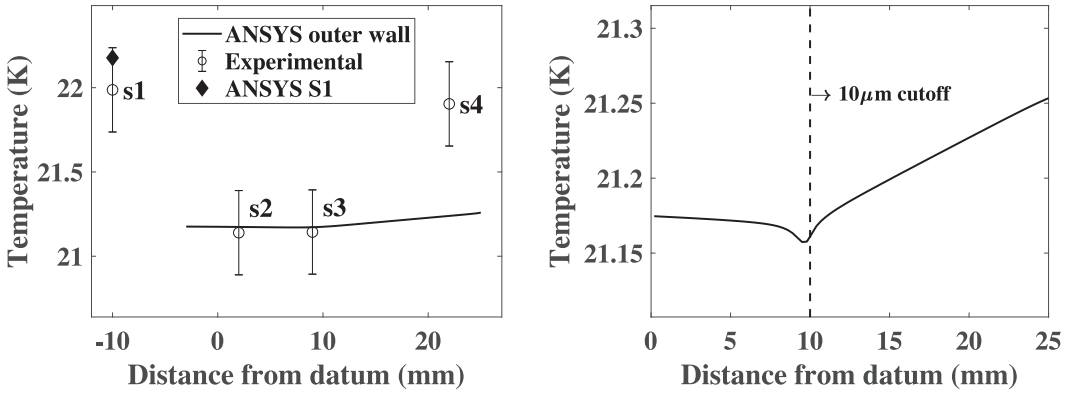

Fig. 10. Temperature distributions along the exterior and interior of the test cell. The datum is located at the bottom of the test cell as shown in Fig. 1(b). Sensor s4 deviation due to 0.5 K bias error in the measurement. The contact line is located at 10 mm.

distributions. The outer wall temperature predictions match the experimentally measured values during this test. The predicted temperature gradient between the contact line location and the flange provides the rate of heat conduction from the heater. The thermal model also provides the rate of heat conduction through the helium exchange gas on the liquid side of the test cell. The inner wall temperature distribution exhibits a large gradient in the contact line region, which will likely result in unanticipated thermocapillary stresses during evaporation. Predictions by this thermal model will enable relaxation of the constant wall temperature boundary condition. The more accurate thermal boundary conditions will allow for deeper investigations into the kinetic model and the underlying physics of phase change.

8. Disclaimer

Certain trade names and company products are mentioned in the text or identified in an illustration in order to adequately specify the experimental procedure and equipment used. In no case does such identification imply recommendation or endorsement by the National Institute of Standards and Technology, nor does it imply that the products are necessarily the best available for the purpose.

Acknowledgments

This work was supported by an Early Stage Innovations Grant from NASA's Space Technology Research Grants Program (Grant # NNX14AB05G). Superior, a high-performance computing infrastructure at Michigan Technological University, was used in obtaining results presented in this publication. Support for this work was also provided to K. Bellur by the Michigan Tech Department of Mechanical Engineering – Engineering Mechanics and through a Michigan Tech Winnikow Fellowship.

References

[1] Panzarella C, Kassemi M. On the validity of purely thermodynamic descriptions of two-phase cryogenic fluid storage. J Fluid Mech 2003;484:41–68.
[2] Panzarella C, Plachta D, Kassemi M. Pressure control of large cryogenic tanks in microgravity. Cryogenics 2004;44:475–83.
[3] Panzarella C, Kassemi M. Self-pressurization of large spherical cryogenic tanks in space. J Spacecr Rock 2005;42:299–308.
[4] Barsi S, Kassemi M, Panzarella C, Alexander JID. A tank self-pressurization experiment using a model fluid in normal gravity. AIAA-2005-1143; January 2005.
[5] Hertz H. Ueber die verdunstung der flüssigkeiten, insbesondere des quecksilbers, im luftleeren raume. Annalen der Physik 1882;253:177–93.
[6] Schrage RW. A theoretical study of interphase mass transfer. Columbia University Press; 1953.
[7] Knudsen M. Maximum rate of vaporization of mercury. Ann Phys 1915;47:697–705.
[8] Barsi S, Kassemi M. Investigation of tank pressurization and pressure controlpart II: numerical modeling. J Therm Sci Eng Appl 2013;5:041006.
[9] Barsi S, Kassemi M. Numerical simulations of the zero boil-off tank experiment. In: 46th AIAA aerospace sciences meeting and exhibit; 2008. p. 810.
[10] Alberts S, Srikanth P, Collicott SH, Heister S. Experiment design for measuring accommodation coefficients for modeling of long-duration spaceflight cryogenic propellants. In: 13th International energy conversion engineering conference; 2015. p. 4246.
[11] Alberts S, Srikanth P, Collicott SH, Heister S. Numerical approach to measure accommodation coefficients for long-duration spaceflight cryogenic propellants. In: 52nd AIAA/SAE/ASEE joint propulsion conference; 2016. p. 4675.
[12] Bellur K, Mdici E, Kulshreshtha M, Konduru V, Tyrewala D, Tamilarasan A, et al. A new experiment for investigating evaporation and condensation of cryogenic propellants. Cryogenics 2016;74:131–7.
[13] Panzarella C, Kassemi M. One-dimensional model of evaporation and condensation in the presence of a noncondensable gas with applications to cryogenic fluid storage. Int J Heat Mass Transf 2009;52:3767–77.
[14] Ajaev V. Interfacial fluid mechanics. Springer; 2012.
[15] Plawsky JL, Ojha M, Chatterjee A, Wayner PC. Review of the effects of surface topography, surface chemistry, and fluid physics on evaporation at the contact line. Chem Eng Commun 2008;196:658–96.
[16] DasGupta S, Kim IY, Wayner PC. Use of the Kelvin-Clapeyron equation to model an evaporating curved microfilm. J Heat Transf 1994;116:1007–15.
[17] Holm F, Goplen S. Heat transfer in the meniscus thin-film transition region. J Heat Transf 1979;101:543–7.
[18] Wee SK, Kihm KD, Pratt DM, Allen JS. Microscale heat and mass transport of evaporating thin film of binary mixture. J Thermophys Heat Transf 2006;20:320–6.
[19] Potash M, Wayner PC. Evaporation from a two-dimensional extended meniscus. Int J Heat Mass Transf 1972;15:1851–63.
[20] Fritz III DL. Implementation of a phenomenological evaporation model into a porous network simulation for water management in low temperature fuel cells. PhD thesis, Michigan Technological University; 2012.
[21] Derjaguin BV, Nerpin SV, Churaev NV. Effect of film transfer upon evaporation of liquids from capillaries. Bull Rilem 1965;29:93–8.
[22] DasGupta S, Schonberg J, Wayner P. Investigation of an evaporating extended meniscus based on the augmented young-laplace equation. Trans – Am Soc Mech Eng J Heat Transf 1993;115:201.
[23] Biswal L, Som S, Chakraborty S. Thin film evaporation in microchannels with slope- and curvature-dependent disjoining pressure. Int J Heat Mass Transf 2013;57:402–10.
[24] Morris S. The evaporating meniscus in a channel. J Fluid Mech 2003;494:297–317.
[25] Hanchak MS, Vangsness MD, Byrd LW, Ervin JS. Thin film evaporation of n-octane on silicon: experiments and theory. Int J Heat Mass Transf 2014;75:196–206.
[26] Akkuş Y, Dursunkaya Z. A new approach to thin film evaporation modeling. Int J Heat Mass Transf 2016;101:742–8.
[27] Schonberg J, DasGupta S, Wayner P. An augmented young-laplace model of an evaporating meniscus in a microchannel with high heat flux. Exp Therm Fluid Sci 1995;10:163–70.
[28] Stephan P, Busse C. Analysis of the heat transfer coefficient of grooved heat pipe evaporator walls. Int J Heat Mass Transf 1992;35:383–91.
[29] Bellur K, Konduru V, Medici EF, Hussey DS, Jacobson DL, LaManna JM, et al. Visualization of the evaporation and condensation phenomena in cryogenic propellants. J Flow Visual Image Process 2016;23:137–56.
[30] Marquardt E, Le J, Radebaugh R. Cryogenic material properties database. Cryocoolers 11. Springer; 2002. p. 681–7.
[31] Mann D. LNG materials and fluids., National Bureau of Standards, Boulder, Colo. 80302. 1977, Sections paged separately (Book); 1977.
[32] Simon N, Drexler E, Reed R. Nist monograph 177 properties of copper and copper alloys at cryogenic temperature. US Government printing Office 1992:2–27.
[33] Touloukian Y, Ho C. Thermophysical properties of selected aerospace materials. Part 2. Thermophysical properties of seven materials, technical report, DTIC Document; 1977.
[34] Ekin J. Experimental techniques for low-temperature measurements: cryostat design, material properties and superconductor critical-current testing. Oxford University Press; 2006.
[35] Hands B, Arp V. A correlation of thermal conductivity data for helium. Cryogenics 1981;21:697–703.
[36] McCarty RD, Arp VD. A new wide range equation of state for helium. In: Advances in cryogenic engineering. Springer; 1990. p. 1465–75.
[37] Arp VD, McCarty RD. Thermophysical properties of helium-4 from 0.8 to 1500 K with pressures to 2000 MPa; 1989.
[38] McCarty RD, Hord J, Roder H. Selected properties of hydrogen (engineering design data). Final report, Technical Report, National Engineering Lab. (NBS), Boulder, CO (USA); 1981.
[39] Liley P, Desai P. Thermophysical Properties of Refrigerants: (inch-pound Edition), ASHRAE; 1993.
[40] Leachman JW, Jacobsen RT, Penoncello S, Lemmon EW. Fundamental equations of state for parahydrogen, normal hydrogen, and orthohydrogen. J Phys Chem Ref Data 2009;38:721–48.
[41] Bellur K, Konduru V, Kulshrestha M, Tyrewala D, Médici EF, Allen JS, et al. Contact angle measurement of liquid hydrogen in stainless steel and aluminum cells. J Heat Transf 2016;138:020904.